

Coherent Phonons and Quasiparticle Renormalization in Semimetals from First Principles

Christoph Emeis,¹ Stephan Jauernik,² Sunil Dahiya,² Yiming Pan,¹
 Carl E. Jensen,² Petra Hein,² Michael Bauer,^{2,3} and Fabio Caruso^{1,3}

¹*Institute of Theoretical Physics and Astrophysics, Kiel University, 24118 Kiel, Germany*

²*Institute of Experimental and Applied Physics, Kiel University, 24118 Kiel, Germany*

³*Kiel Nano, Surface and Interface Science KiNSIS, Kiel University, 24118 Kiel, Germany*

Coherent phonons, light-induced coherent lattice vibrations in solids, provide a powerful route to engineer structural and electronic degrees of freedom using light. In this manuscript, we formulate an ab initio theory of the displacive excitation of coherent phonons (DECP), the primary mechanism for light-induced structural control in semimetals. Our study – based on the ab initio simulations of the ultrafast electron and coherent-phonon dynamics in presence of electron-phonon interactions – establishes a predictive computational framework for describing the emergence of light-induced structural changes and the ensuing transient band-structure renormalization arising from the DECP mechanism. We validate this framework via a combined theoretical and experimental investigation of coherent phonons in the elemental semimetal antimony. Via a Fourier analysis of time- and angle-resolved photoemission spectroscopy (tr-ARPES) measurements, we retrieve information about transient spectral features and quasiparticle renormalization arising from the coherent A_{1g} phonon as a function of momentum, energy, time, and fluence. The qualitative and quantitative agreement between experiment and theory corroborates the first-principles approach formulated in this study. Besides advancing the fundamental understanding of electron-phonon interactions mediated by coherent phonons, this study opens new opportunities for predictively engineering structural and electronic degrees of freedom in semimetals via the DECP mechanism.

I. INTRODUCTION

Coherent phonons refer to the damped oscillations experienced by a crystalline lattice following a time-dependent perturbation, and they are a direct manifestation of light-induced structural changes in photo-excited solids. They were first observed in the early 1990s in pump-probe transient-reflectivity measurements of elemental semimetals [1, 2] and since then they have been detected and characterized in various material families using a range of spectroscopy techniques [3–10]. In addition to time-resolved optical and scattering probes, coherent phonons have also been observed in tr-ARPES studies in a wide range of different materials [11–19]. This technique stands out for its ability to study the coupling of coherent phonons to the electronic degrees of freedom in an exceptionally direct, momentum- and energy-resolved manner. The recent development of frequency-domain angle-resolved photoemission spectroscopy (FD-ARPES) allows for a mode-resolved tracking of band-structure renormalization effects caused by coherent phonons [20–24]. Via a Fourier analysis, the contributions of individual modes to changes in the band structure can be disentangled, providing unprecedented information on electron-phonon interactions mediated by coherent phonons with energy, momentum, and phonon frequency resolution.

The fundamental interests in coherent phonons is motivated by the wide possibilities they offer to directly tailor specific materials properties – as e.g. magnetism [25–28], ferroelectricity [29–32], topology [14, 15, 33], and superconductivity [10, 34–36]. Additionally, they can serve as a precursor to drive light-induced phase transi-

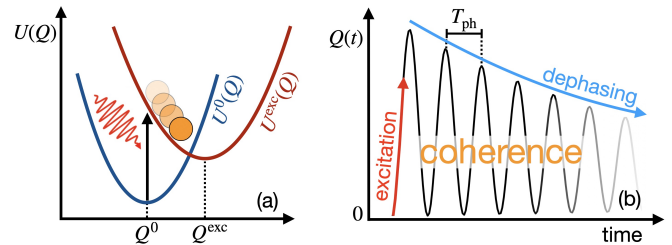


FIG. 1. (a) Schematic representation of the DECP mechanism. U^0 (U^{exc}) denotes the ground-state (excited-state) potential-energy surface before (after) photoexcitation. Q is an adimensional collective displacement amplitude of the lattice along a fully-symmetric Raman-active phonon. (b) Characteristic time-dependence of the displacement amplitude Q for the DECP mechanism. Following excitation, the coherent phonon dynamics is characterized by damped oscillations with periodicity set by the phonon period $T_{\text{ph}} = 2\pi\omega_{\text{ph}}^{-1}$.

tions [16, 37, 38], or to access hidden-metastable states inaccessible under equilibrium conditions [39, 40]. Coherent phonons can be launched via a variety of excitation pathways, including inelastic stimulated Raman scattering, ionic Raman scattering, infrared absorption, and the displacive excitation of coherent phonons (DECP) [41–47]. Among these, the DECP mechanism constitutes the primary excitation pathway for semimetals and it can play an important role in photo-excited semiconductors.

In the DECP mechanism, the coherent motion of the lattice is triggered by modifications of the electron-density distribution due to photoabsorption [42]. Carrier photoexcitation results into a quasi-adiabatic displacement of the potential energy surface, as depicted in

Fig. 1 (a), triggering damped lattice oscillations around the new minimum with the characteristic oscillatory pattern illustrated in Fig. 1 (b). Phenomenological models can be designed to reproduce targeted experimental fingerprints arising from these phenomena [48]. Yet, they are inherently dependent on experimental observation, and they are unsuitable to capture the coherent phonon spectrum in structurally complex compounds. However, predictive and transferable atomistic models for the DECP mechanism in semimetals have not yet been presented. The challenge in developing a first-principles theory of DECP is twofold: First, it is necessary to describe the coherent phonon excitation induced by dynamical changes of the electron density. Second, one must consider the resulting band structure renormalization, which arises from the electron-phonon interactions mediated by the driven coherent phonons within a perturbative many-body framework.

In this manuscript, we formulate an ab initio theory for the DECP mechanism in semimetals. Our approach specifically targets (i) the emergence of photo-induced coherent lattice motion following electronic excitation by a pump pulse and (ii) transient band-structure renormalization effects induced by coherent phonons. The former is obtained via the joint solution of the coherent-phonon equation of motion (EOM) alongside with the time-dependent Boltzmann equation (TDBE)[49–52] – the state of the art for ab initio simulations of the joint ultrafast dynamics of electrons and phonons. Band-structure renormalization effects are accounted for within an adiabatic many-body formulation of quasiparticle corrections due to coherent phonons. We assess the predictive power of this approach against tr-ARPES measurements for antimony, whereby we characterize the emergence of coherent phonons and their impact on the electron band structure as a function of energy, momentum, time, and pump fluence. The predictive power of this theoretical framework, demonstrated by the robust agreement between theory and experiments, opens up new opportunities to predictively engineer structural and electronic degrees of freedom in non-equilibrium conditions.

The manuscript is structured as follows. In Sec. II, we introduce the theoretical framework for the first-principles description of coherent phonons. Details of the tr-ARPES measurements and the FD-ARPES technique are reported in Sec. III. In Sec. IV, the equilibrium electronic and vibrational properties of antimony and their fingerprints in tr-ARPES measurements are reviewed. Measurements and ab initio calculations of band-structure renormalization induced by coherent phonons in antimony are presented in Sec. V, and their fluence dependence is analyzed in Sec. VI. Discussions and an outlook are presented in Sec. VII. Our concluding remarks are reported in Sec. VIII.

II. THEORY

In the following, we proceed to introduce a theoretical framework suitable to capture the emergence of coherent phonons in semimetals based on first-principles electronic-structure calculations.

A first-principles description of coherent phonons requires tracking the time dependence of the displacement $\Delta\tau_{\kappa p}(t)$ of the κ -th nucleus in the p -th unit cell from its equilibrium coordinate in presence of an external time-dependent perturbation (as, e.g., a driving field). $\Delta\tau_{\kappa p}$ can be quantized by introducing a normal mode basis, leading to [53]:

$$\Delta\hat{\tau}_{\kappa p} = \sum_{\mathbf{q}\nu} \left(\frac{\hbar}{2\omega_{\mathbf{q}\nu}M_{\kappa}} \right)^{\frac{1}{2}} e^{i\mathbf{q}\cdot\mathbf{R}_p} \mathbf{e}_{\mathbf{q}\nu}^{\kappa} \hat{Q}_{\mathbf{q}\nu} \quad . \quad (1)$$

Here, $\hat{Q}_{\mathbf{q}\nu} = N_p^{-\frac{1}{2}}(\hat{a}_{\mathbf{q}\nu} + \hat{a}_{-\mathbf{q}\nu}^{\dagger})$ is an adimensional coherent-phonon amplitude that quantifies the lattice distortion along the $\mathbf{q}\nu$ normal mode. $\hat{a}_{\mathbf{q}\nu}$ and $\hat{a}_{\mathbf{q}\nu}^{\dagger}$ denote annihilation and creation bosonic operators, respectively. N_p is the number of \mathbf{q} points, M_{κ} the nuclear mass, $\omega_{\mathbf{q}\nu}$ the phonon frequency for crystal momentum \mathbf{q} and mode index ν . $\mathbf{e}_{\mathbf{q}\nu}^{\kappa}$ denotes phonon eigenvectors, and \mathbf{R}_p crystal-lattice vectors.

For the DECP mechanism, this problem can be addressed via the solution of the Heisenberg EOM for $\hat{Q}_{\mathbf{q}\nu}$, namely $\partial_t^2 \hat{Q}_{\mathbf{q}\nu}(t) = -\hbar^{-2} [[\hat{Q}_{\mathbf{q}\nu}, \hat{H}], \hat{H}]$ where $\hat{H} = \hat{H}_{\text{ph}} + \hat{H}_{\text{eph}}$ is the total lattice Hamiltonian, consisting of the non-interacting phonon Hamiltonian $\hat{H}_{\text{ph}} = \sum \hbar\omega_{\mathbf{q}\nu}(\hat{a}_{\mathbf{q}\nu}^{\dagger}\hat{a}_{\mathbf{q}\nu} + 1/2)$ and the electron-phonon interaction $\hat{H}_{\text{eph}} = \sum g_{mn}^{\nu}(\mathbf{k}, \mathbf{q}) [\hat{c}_{m\mathbf{k}+\mathbf{q}}^{\dagger}\hat{c}_{n\mathbf{k}} - \delta_{nm}\delta_{\mathbf{q}0}] \hat{Q}_{\mathbf{q}\nu}$. The second term in brackets, recently introduced in Ref. [54], is critical to correctly capture the coherent phonon excitation. Here, $g_{mn}^{\nu}(\mathbf{k}, \mathbf{q})$ is the electron-phonon coupling matrix element, $\hat{c}_{n\mathbf{k}}$ and $\hat{c}_{n\mathbf{k}}^{\dagger}$ are fermionic annihilation and creation operators, respectively, and the sums extend over all the indices of the arguments.

Making use of standard commutation relations, one promptly arrives at the EOM for the coherent-phonon amplitude [47]:

$$\partial_t^2 Q_{\nu} + \omega_{\nu}^2 Q_{\nu} = -\omega_{\nu} \hbar^{-1} \sum_{n\mathbf{k}} g_{nn}^{\nu}(\mathbf{k}, 0) \Delta f_{n\mathbf{k}}(t) \quad , \quad (2)$$

$\Delta f_{n\mathbf{k}} = f_{n\mathbf{k}}(t) - f_{n\mathbf{k}}^{(0)}$, and $f_{n\mathbf{k}}^{(0)}$ is the (equilibrium) Fermi-Dirac distribution before excitation, whereas $f_{n\mathbf{k}}(t)$ denotes the non-equilibrium distribution function at time t . The dependence on \mathbf{q} is omitted, as selection rules require $\mathbf{q} = 0$. This expression has been derived by neglecting electron coherence ($\langle \hat{c}_{m\mathbf{k}+\mathbf{q}}^{\dagger}\hat{c}_{n\mathbf{k}} \rangle \simeq f_{n\mathbf{k}}$), which is justified for timescales of the order of 50 fs and longer. The inclusion of non-diagonal contributions to the density matrix and their influence on the coherent phonon dynamics can be handled within the framework of non-equilibrium Green function, as recently demonstrated in

the study of exciton-phonon interactions in monolayer MoS₂ [55].

Numerical evaluation of Eq. (2) requires knowledge of the time-dependent occupation function $f_{n\mathbf{k}}(t)$ whose time-dependence is governed by the time-dependent Boltzmann equation (TDBE) [49, 51]:

$$\partial_t f_{n\mathbf{k}} = \Gamma^{\text{e-ph}} [f_{n\mathbf{k}}, n_{\mathbf{q}\nu}] + \Gamma^{\text{e-e}} [f_{n\mathbf{k}}] \quad , \quad (3)$$

$$\partial_t n_{\mathbf{q}\nu} = \Gamma^{\text{ph-e}} [f_{n\mathbf{k}}, n_{\mathbf{q}\nu}] \quad . \quad (4)$$

Here, $n_{\mathbf{q}\nu}$ denotes the phonon distribution function, and $\Gamma^{\text{e-ph}}$, $\Gamma^{\text{e-e}}$, and $\Gamma^{\text{ph-e}}$ are the collision integrals due to electron-phonon, electron-electron, and phonon-electron scattering, respectively, for which explicit expressions can be found elsewhere [51, 56].

Equations (2)-(4) form a set of coupled integro-differential equations, which can be solved by conventional time-propagation algorithms (e.g., Heun's method or fourth-order Runge-Kutta) to determine the coherent-phonon amplitude Q_ν alongside with the electron ($f_{n\mathbf{k}}$) and phonon distribution functions ($n_{\mathbf{q}\nu}$). In this work, we solve Eqs. (2)-(4) within the EPW code [57] as an initial value problem to determine the coupled dynamics of electrons and coherent phonons in semimetals following excitation with a pump pulse. As initial conditions, we consider electronic excited states representative of the conditions established in a pump-probe experiment, and described by a high-temperature Fermi-Dirac distribution $f_{n\mathbf{k}}(t=0) = [\exp(\varepsilon_{n\mathbf{k}} - \mu)/k_B T_{\text{exc}} + 1]^{-1}$, where the excitation temperature T_{exc} is set to match the estimated incident pump fluence in the tr-ARPES measurements (see discussion in Appendix B). All quantities required in the evaluation of Eqs. (2)-(4) are obtained from first principles via density-functional theory (DFT) [58, 59] and density-function perturbation theory (DFPT) [60]. In particular, we first obtain electron energies $\varepsilon_{n\mathbf{k}}$ from DFT, phonon frequencies $\omega_{\mathbf{q}\nu}$ and electron-phonon coupling matrix elements $g_{nm}^\nu(\mathbf{k}, \mathbf{q})$ from DFPT. All quantities are interpolated on dense momentum grids using maximally-localized Wannier function [61, 62] within the EPW and Wannier90 codes [63]. We thus proceed to solve Eqs. (2)-(4) by time-stepping the time derivative via the second-order Runge-Kutta algorithm (Heun method) for a total duration of 3 ps with time steps of 1 fs. The last step of this procedure involves the calculations of quasiparticle corrections due to coherent phonons, which is detailed in Sec. V. A schematic illustration of this workflow is reported in Fig. 2, whereas a detailed description of computational parameters is provided in Appendix A.

Equation (2) is reminiscent of the EOM for a driven harmonic oscillator, with a driving term $D_{\text{eph}}(t) = -\omega_\nu \hbar^{-1} \sum_{n\mathbf{k}} g_{nn}^\nu(\mathbf{k}, 0) \Delta f_{n\mathbf{k}}(t)$. A necessary condition for the excitation of coherent phonons is $D_{\text{eph}}(t) \neq 0$. Equation (2) thus reveals that coherent excitation of the ν -th zone-center phonon can only occur if $g_{nn}^\nu(\mathbf{k}, 0) = \langle u_{n\mathbf{k}} | \Delta_\nu \hat{v}_{\text{KS}} | u_{n\mathbf{k}} \rangle \neq 0$, where $\Delta_\nu v_{\text{KS}}$ is the linear change of the Kohn-Sham potential and $u_{n\mathbf{k}}$ is the cell-periodic part of a Bloch state. Simple group-theoretic considerations indicate that this condition can only be obeyed

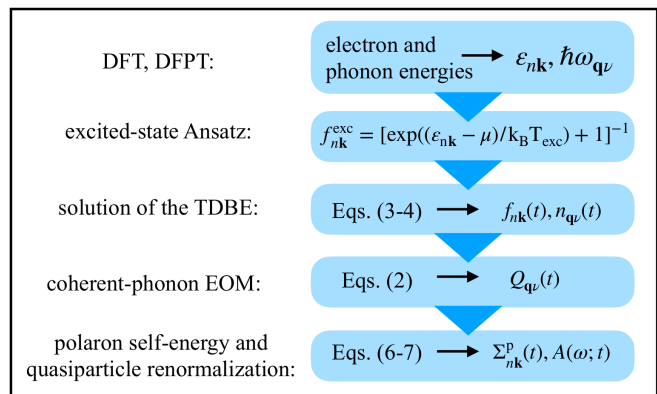


FIG. 2. Workflow for the ab initio investigations of coherent phonons in semimetals.

if the irreducible representation of the ν -th phonon contains the totally symmetric representation of the lattice (namely, $\Gamma_\nu \supseteq A_{1g}$). In short, only totally-symmetry Raman-active modes – as, e.g., the A_{1g} phonons in Sb – can be coherently excited via the DECP mechanism. This condition constitutes an important selection rule for coherent-phonon excitation in semimetals.

III. TIME-RESOLVED AND FREQUENCY-DOMAIN ARPES

In the following, we proceed with the details of the tr-ARPES measurements and the FD-ARPES technique. Details of the experimental setup are described in Ref. [64]. For the experiments, we used Sb single crystals with a (111) surface orientation. Tr-ARPES measurements were performed at a time resolution of ≈ 100 fs (FWHM of pump-probe cross-correlation) using 1.48 eV, sub-30 fs pump pulses and 5.90 eV, 95 fs probe pulses focused on the sample surface at an angle of incidence of 45° . The horizontal and vertical size of the pump (probe) beam at the sample surface was $237 \times 180 \mu\text{m}^2$ ($43 \times 70 \mu\text{m}^2$) in full width at half maximum. The plane of incident was the $\overline{\Gamma\text{K}}$ plane of the Sb(111) surface Brillouin zone (BZ) and both pump and probe light polarization were oriented parallel to this plane. The incident pump fluence on the sample was varied between 0.04 mJ cm^{-2} and 0.26 mJ cm^{-2} corresponding to absorbed fluences between 0.016 mJ cm^{-2} and 0.10 mJ cm^{-2} [65]. Photoelectrons were collected with a hemispherical analyzer along the $\overline{\Gamma\text{K}}$ direction with a total energy resolution of 35 meV. The sample quality was checked by low-energy electron diffraction and the sample was simultaneously aligned in the $\overline{\Gamma\text{K}}$ direction for the tr-ARPES measurements. In the ARPES data a sharp signature of the surface band is another indicator for a good sample preparation. All experiments were performed at room temperature at a pressure of $< 2 \times 10^{-10}$ mbar.

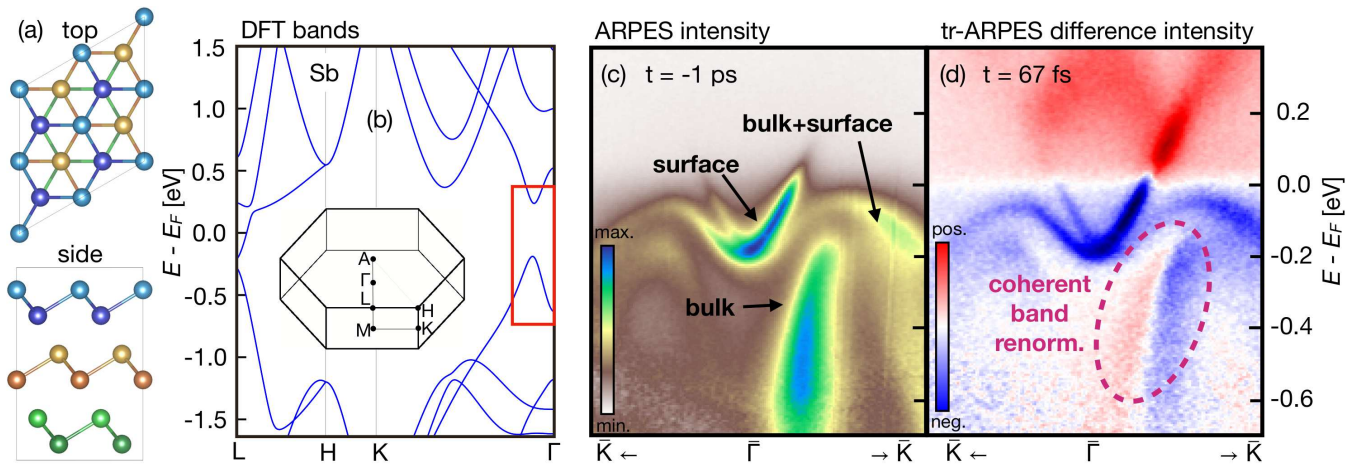


FIG. 3. (a) Top and side view of the crystal structure of Sb. (b) Electron bulk band structure along the L-H-K- Γ high-symmetry path in the BZ as obtained from DFT. The hexagonal non-primitive BZ of Sb is shown as an inset and energies are relative to the Fermi energy. (c) Static ARPES spectrum I_0 obtained before photoexcitation for energies and crystal momenta within the red rectangle in panel (b). In addition to bulk bands, measurements reveal surface states and bands of hybrid surface-bulk character (not shown in panel (b)). (d) Difference-intensity tr-ARPES spectrum $\Delta I(t) = I(t) - I_0$ for a time delay of 67 fs and an excitation fluence of 0.26 mJ cm^{-2} . Red (blue) denotes intensity gain (loss). The dashed oval marks the energy and momentum region exhibiting pronounced transient band-structure renormalizations due to coupling with coherent phonons.

The tr-ARPES data were taken in a total (pump-probe) time delay range of ≈ 2.75 ps with a sampling rate of 60 THz to comply with the Nyquist sampling criterion for probing the A_{1g} mode. For the energy- and momentum-resolved Fourier analysis, we divided the tr-ARPES intensity maps into small integration regions of $6 \text{ meV} \times 0.0022 \text{ \AA}^{-1}$. Each of these regions exhibits a photoemission intensity transient showing a superposition of carrier population dynamics and coherent-phonon-induced modulations. To separate the two signal contributions, we fitted the transients with a fifth-order polynomial (starting at a time delay of 33 fs) to model the carrier relaxation dynamics. By subtracting the fitting results from the transients, the oscillatory part of the signal can be extracted (see also Supplementary Figure S6). The resulting transients were zero-padded to triple their lengths before their amplitude spectra were determined via fast Fourier transformation. This results in a data set of energy- and momentum-dependent Fourier amplitude spectra (with a frequency increment of 0.12 THz). FD-ARPES spectra are cuts through this data set at a fixed frequency representing the energy- and momentum-resolved Fourier amplitude at the selected frequency.

IV. ELECTRONIC PROPERTIES AND COHERENT PHONONS IN ANTIMONY

Antimony (Sb) is an elemental semimetal which crystallizes in a rhombohedral lattice, illustrated in Fig. 3 (a), consisting of 2 atoms per unit cell and belonging to the $R\bar{3}m$ crystallographic group [66]. Owing to its simplicity and the existence of a well-defined coherent phonon spec-

trum, it constitutes an ideal test case for the benchmark and validation of the ab initio approach formulated in this manuscript. In particular, at the Γ point the phonon dispersion obtained from DFPT (Supplementary Figure S2) is characterized by a non-degenerate totally-symmetric A_{1g} mode and one doubly-degenerate E_g mode with frequencies of 4.4 and 3.2 THz, respectively, which slightly underestimate the experimental values (4.5 and 3.5 THz). Coherent phonons of both A_{1g} and E_g characters can be excited in Sb, however, only the former obeys symmetry selection rules required to undergo excitation via the DECP mechanism. Conversely, coherent E_g phonons require alternative excitation pathways (as, e.g., ionic Raman scattering and inelastic stimulated Raman scattering), which are higher-order in the interaction [67].

The DFT-PBE band structure along the L-H-K- Γ path is reported in Fig. 3 (b). Here and below, we consider the non-primitive hexagonal unit cell (6 atoms per cell) and BZ (illustrated in the inset of Fig. 3 (b)), as this choice enables the straightforward identification of the high-symmetry path probed by tr-ARPES on the (111) surface. A comparison of the primitive and non-primitive structures and BZ is included in Supplementary Figure S2 [68]. The Fermi surface is located in the vicinity of the L point and the red rectangle marks the region probed by the tr-ARPES measurements. The static ARPES intensity I_0 along the K- Γ -K path is reported in Fig. 3 (c) before photoexcitation. The spectral features are in good agreement with previous experimental works [69, 70] and reveal photoemission signatures of different origins: one bulk band – well captured by the bulk DFT calculation – as well as surface and hybrid surface-bulk bands. The interfacial origin of these spectral features is

corroborated by comparison with DFT simulations for a finite slab consisting of 16 Sb layers (see Supplementary Figure S3 [68]).

In Fig. 3 (d), we report the tr-ARPES difference intensity $\Delta I(t) = I(t) - I_0$ for a time delay of $t = 67$ fs after excitation. Red (blue) colors denote intensity gain (loss). For energies larger than -0.2 eV, the gain-loss pattern predominantly reflects carrier photoexcitation above the Fermi energy, with the ensuing depopulation of lower-energy states. In the region within the dashed oval in Fig. 3 (d) we further observe transient intensity renormalizations that are indicative of the excitation of coherent phonons. These gain-loss patterns arise from the upward-downward shifting of the bulk band, and oscillate with a characteristic frequency that coincides with the A_{1g} mode frequency. These band oscillations are further illustrated in Supplementary Figure S6 and in the Supplementary Video [68]. These spectral fingerprints are a direct manifestation of electron-phonon interactions involving the bulk Sb band and the coherently-driven A_{1g} mode, and their dynamics reflects the transient band-structure renormalization driven by a photo-induced structural change.

V. QUASIPARTICLE RENORMALIZATION VIA COHERENT PHONONS IN ANTIMONY

To describe the coherent phonon dynamics triggered by an electronic excitation in Sb, we solve Eqs. (2)-(4) from first principles and determine the time-dependent coherent-phonon amplitude Q_ν . This procedure has been applied to all zone-center optical phonons of Sb. Only the A_{1g} mode displays coherent dynamics, whereas the E_g modes do not satisfy the symmetry selection rules outlined in Sec. II, leading to vanishing coherent amplitude.

The electron distribution function $f_{n\mathbf{k}}$ derived from the solution of Eqs. (3) and (4) is illustrated in Supplementary Figure S4 [68]. The calculated coherent-phonon amplitude $Q_{A_{1g}}$ for the A_{1g} mode is marked in blue in Fig. 4 (a). It is characterized by periodic and damped cosine-like oscillations, with an oscillation period equal to the phonon period $T_\nu = 2\pi\omega_\nu^{-1} = 0.22$ ps. In the simulations, we explicitly account for coherent-phonon damping due to the phonon-phonon interaction [71] via the scattering rate $\gamma_\nu = 0.5$ ps $^{-1}$. This quantity is estimated from ab initio finite-difference calculations of the third-order force constant tensor (see Appendix A) and it is accounted for by inclusion of a term $\gamma_\nu \partial_t Q_\nu$ in the left-hand side of Eq. (2). For comparison, Fig. 4 (a) further illustrates the time-dependent modulation of the tr-ARPES signal averaged over the spectral region marked by the black rectangle in Fig. 4 (d). The experimental curves in Fig. 4 (a) have been scaled to match the amplitude of the first maximum of the calculated coherent phonon amplitude. The oscillation frequencies and damping of the tr-ARPES data agree well with ab initio simulations. Our

results are further consistent with timescales of coherent-phonon damping revealed by earlier experimental studies and further support the identification of phonon-phonon scattering as the primary source of damping [72–74].

We further illustrate in Fig. 4 (b) the Fourier transform of the calculated and measured coherent-phonon oscillations from panel (a). The Fourier analysis confirms that the frequency of the A_{1g} mode dominates the coherent-phonon oscillations. Additionally, Fig. 4 (b) indicates that the peak broadening of the calculated Fourier amplitude agrees well with the measurements consolidating the interpretation of phonon-phonon scattering as the primary mechanism for coherent-phonon damping.

In the following, we proceed to describe band-structure renormalization effects mediated by coherent phonons within a perturbative many-body framework. Under equilibrium conditions, the phonon-assisted renormalization of the electron-band structures is well understood and it provides the basis for understanding the temperature dependence of the electronic properties of solids. At equilibrium, quasiparticle energies are renormalized by the inclusion of a self-energy correction [53]:

$$\varepsilon_{n\mathbf{k}}^{\text{QP}} = \varepsilon_{n\mathbf{k}} + \text{Re}\Sigma_{n\mathbf{k}}(\varepsilon_{n\mathbf{k}}^{\text{QP}}) \quad . \quad (5)$$

Here, $\Sigma_{n\mathbf{k}}$ is the electron self-energy due to the electron-phonon interaction, which includes the Fan-Migdal Σ^{FM} and Debye-Waller Σ^{DW} terms. In presence of light-induced structural changes, an additional self-energy term contribute to the band structure renormalization [54, 75, 76]:

$$\Sigma_{n\mathbf{k}}^p(t) = \sum_{\mathbf{q}\nu} g_{nn}^\nu(\mathbf{k}, \mathbf{q}) Q_{\mathbf{q}\nu}(t) \quad . \quad (6)$$

This term arises from the perturbative correction of the single-particle eigenvalues at first-order in the electron-phonon interaction. While it exactly vanishes at equilibrium ($Q_{\mathbf{q}\nu} = 0$), this term is directly responsible for the band-structure renormalization due coherent phonons. We point out that Eq. (6) is formally identical to the polaron self-energy introduced in the many-body polaron theory [75, 77], and its appearance is also consistent with a formulation of the coupled electron-phonon dynamics based on non-equilibrium Green's functions [54, 76]. For consistency with earlier works, we therefore refer to Eq. (6) as the polaron self-energy.

In order to account for coherent-phonon renormalization of the electronic properties, we evaluate the time-dependent electron spectral function according to:

$$A(\omega, t) = \sum_{n\mathbf{k}} \frac{\pi^{-1} \text{Im} \Sigma_{n\mathbf{k}}}{[\hbar\omega - \varepsilon_{n\mathbf{k}} - \text{Re} \Sigma_{n\mathbf{k}}]^2 + [\text{Im} \Sigma_{n\mathbf{k}}]^2} \quad . \quad (7)$$

Here, the total time- and frequency-dependent self-energy is defined as $\Sigma_{n\mathbf{k}}(\omega, t) = \Sigma_{n\mathbf{k}}^{\text{FM}}(\omega) + \Sigma_{n\mathbf{k}}^p(t)$. In short, the spectral function $A(\omega, t)$ accounts for static phonon-assisted renormalization of the band structure via the Fan-Migdal term, whereas time-dependent effects

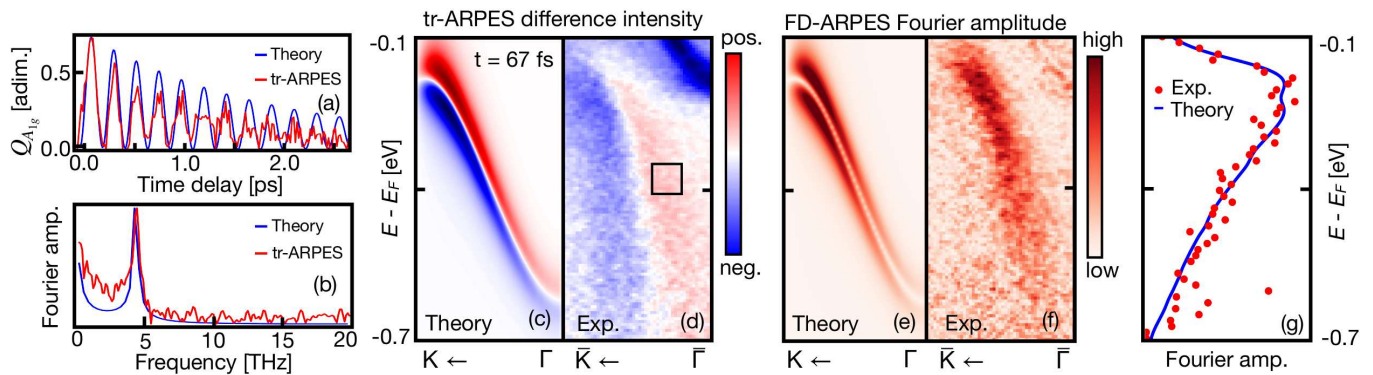


FIG. 4. (a) Displacement amplitude of the A_{1g} mode as obtained from the solution of the coherent-phonon EOM [Eq. (2)]. For comparison, we report the oscillation of the transient tr-ARPES signal taken within a region of interest marked by a black rectangle in (d). (b) Fourier transform of the tr-ARPES signal and the calculated displacement amplitude in (a). Simulations (c) and measurements (d) of changes in the tr-ARPES spectral function at a time delay of 67 fs after photoexcitation for crystal momenta in the vicinity of the Γ point. Red (blue) denotes intensity gain (loss). An incident pump fluence of 0.26 mJ cm^{-2} was considered. Theoretical (e) and experimental (f) FD-ARPES map obtained from the Fourier analysis of the time-resolved spectral functions at the frequency of the A_{1g} -mode of Sb. (e) Comparison between simulations and measurements for the maximum Fourier amplitude in the FD-ARPES map, as a function of energy.

due to coherent phonons are introduced via the polaron self-energy. Similar to earlier studies, the Debye-Waller contribution is approximately accounted for by enforcing particle conservation [78]. We further account for optical selection rules via inclusion of the dipole matrix elements in the spectral function (see discussion in Appendix A 2), and for finite experimental resolution by applying a 40 meV broadening to the spectral function.

Figure 4 (c) displays the calculated transient spectral function $\Delta A(\omega, t) = A(\omega, t) - A(\omega, 0)$ for a time delay of $t = 67 \text{ fs}$ after photo-excitation, which corresponds to the first maximum of the displacement amplitude in Fig. 4 (a). The static spectral function $A(\omega, 0)$ is reported in Supplementary Figure S5 [68]. To determine initial conditions for simulations compatible with experiments, we set the initial excited-state energy in our calculations to match the estimated absorbed pump-energy per unit cell. A detailed discussion of this procedure is provided in the Appendix B. The intensity gain and loss patterns – marked in red and blue, respectively – reflect an upward energy renormalization of the bulk electron band owing to the coupling with the coherent A_{1g} phonon, and it oscillates following the time profile of Fig. 4 (a).

In Fig. 4 (d), we report the measured tr-ARPES transient spectral function at the same time delay t for an incident fluence of 0.26 mJ cm^{-2} . The calculated gain-loss pattern as well as its time dependence are in good agreement with tr-ARPES measurements. In the vicinity of the Fermi energy, the tr-ARPES measurements are sensitive to the surface band, which manifests itself as a high-intensity feature in the top-right corner of Fig. 4 (d) due to photoexcitation of the hybrid surface-bulk band marked in Fig. 3 (c). These features dominate the transient spectral intensity above -0.2 eV below the Fermi energy, overshadowing the energy renormalization of the bulk band. Surface bands, however, couple weakly to

coherent phonons as compared to bulk states, and they exhibit much weaker intensity oscillations [70], as illustrated in Supplementary Figures S6 and S7.

In Figs. 4 (e) and 4 (f), we report the theoretical and experimental FD-ARPES spectra obtained from the Fourier transformation of the tr-ARPES spectral functions for a fluence of 0.26 mJ cm^{-2} . The maximum Fourier amplitude of experiment (theory) is obtained at a frequency $\omega_{\text{exp}} = 4.5 \text{ THz}$ ($\omega_{\text{theo}} = 4.4 \text{ THz}$), which coincides with the oscillation of the A_{1g} mode. Overall, FD-ARPES filters out the spectral features that do not exhibit an oscillatory component, thereby highlighting electronic states that are strongly coupled to the coherent phonons. The intensity of the surface states, conversely, is suppressed owing to their weak coupling to the A_{1g} mode. In Fig. 4 (g), we report the maximum Fourier amplitude as a function of energy. The highest Fourier amplitude is obtained at -0.2 eV and it decreases at lower energies. This trend is well reproduced by our ab initio calculations across the full energy range of the measurements. This behaviour can be attributed to a suppression of the ARPES intensity in the vicinity of the Γ point due to the polarization of the probe pulse and the dipole selection rules for optical transitions (see also Appendix A 2).

VI. FLUENCE-DEPENDENT BAND-STRUCTURE RENORMALIZATION

Having established a predictive ab initio framework for the analysis of coherent phonons in semimetals, we proceed to explore to which extent quasiparticle renormalization effects can be tailored upon control of the external driving field. In particular, we varied the pump-fluence in the tr-ARPES measurements between 0.04 and

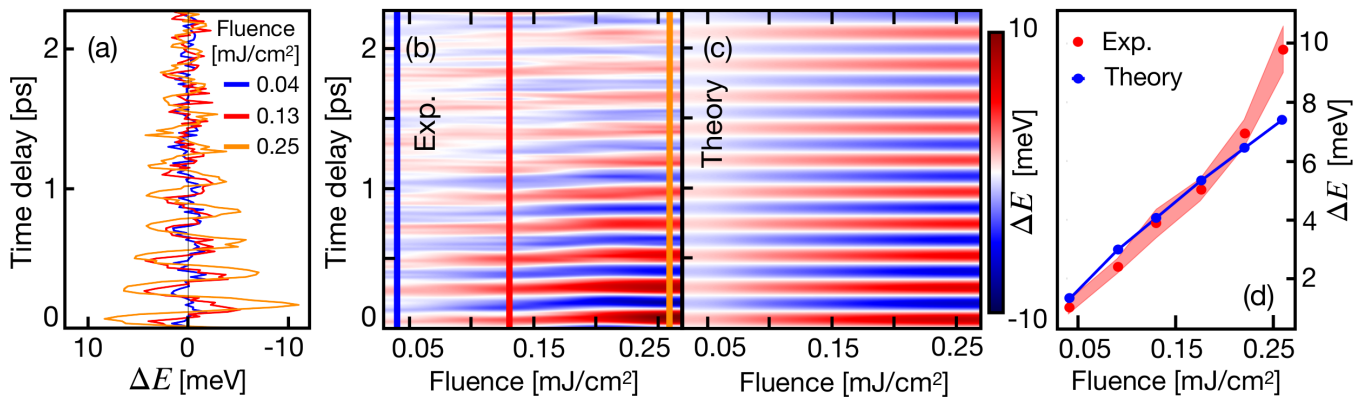


FIG. 5. (a) Momentum-averaged energy renormalization of the bulk band in the vicinity of the Γ point due to coherent phonon excitation for incident fluences of 0.04 (blue), 0.13 (red) and 0.26 mJ cm^{-2} (orange). (b) Momentum-averaged energy renormalization of the bulk band in the vicinity of the Γ point as a function of fluence and time extracted from the tr-ARPES data. The orange, red and blue lines highlight the time-dependent energy renormalization at 0.04, 0.13 and 0.26 mJ cm^{-2} presented in panel (a), respectively. (c) Calculated energy renormalization of the bulk band at Γ as a function of fluence and time obtained from Eq. (6). (d) Maximum energy renormalization versus incident fluence of the theoretical and fitted experimental oscillations.

0.26 mJ cm^{-2} , and investigated its impact on the energy renormalization ΔE due to coherent phonons. Figure 5 (a) illustrates the time-dependent energy renormalization ΔE of the bulk band in the vicinity of the Γ point for fluences of 0.04 (blue), 0.13 (red) and 0.26 mJ cm^{-2} (orange). To focus on the oscillatory component of the band renormalization, we subtracted the non-oscillating component of the transient spectral function following the procedure outlined in the Supplementary Note S1, and illustrated in Supplementary Figure S1 [68]. For all fluences, measurements reveal a periodic renormalization of the band energies and indicate a significant increase of the maximum energy renormalization with the pump fluence.

The full time- and fluence-dependent measurements of the bulk-band renormalization is further illustrated in Fig. 5 (b). The orange, red and blue lines highlight the fluences reported in Fig. 5 (a). In addition to an increase of coherent-phonon energy renormalization with fluence, Fig. 5 (b) further reveals a damping of the oscillations that is not substantially affected by the pump fluence. Figure 5 (c) reports ab initio simulations of fluence- and time-dependent energy renormalizations of the bulk band in the vicinity of the Γ point. Overall, we find very good agreement between experiment and theory across the full range of fluences and time delays. Experimental data further exhibit an increase in softening of the coherent phonon frequency for larger driving fluences. These effects (not captured in the simulations) are reminiscent of phonon renormalization arising in highly-doped semiconductors due to electron-phonon coupling [79, 80]. We thus tentatively attribute these effects to the dressing of the coherent phonons via electron-phonon interactions mediated by the photo-excited carriers, in close analogy to the static counterpart of these effects. To quantitatively compare theory and experiments, we further dis-

play in Fig. 5 (d) the measured and calculated maximum energy renormalization of the bulk band as a function of the incident fluence. Tr-ARPES indicates a linear dependence of the energy renormalization on fluence, which is well reproduced by ab initio calculations. This trend suggests that the driving fluences considered in this work are well captured within the linear-response regime.

A breakdown of the linear regime has been reported in pump-probe Raman experiments for antimony at driving fluences exceeding 5 mJ cm^{-2} [81]. This value constitutes an upper limit for the maximum fluence to excite and probe coherent-phonon band-structure renormalization. By extrapolating the linear trend observed in Fig. 5 (d), we expect that energy renormalizations exceeding 100 meV could be realized at high-driving fields without undergoing structural damage.

VII. DISCUSSION AND OUTLOOK

Overall, the ab initio formalism presented in this manuscript offers new opportunities for predictive simulations of light-induced phenomena in materials and, specifically, for monitoring structural changes and quasiparticle renormalization effects emerging on ultrafast timescales. Some perspectives and opportunities for the application of these concepts beyond the domain of this manuscript are discussed below.

The fluence-dependent analysis reported in Sec. VI indicates that energy renormalization of the order of 10 to 100 meV can be realized in semimetals via experimentally accessible pump fluences. Energy shifts of this magnitude may suffice to tailor specific band-structure features via coherent phonons or even to induce topological features in otherwise topologically trivial compounds. Coherent-phonon excitation in Weyl semimetals, for ex-

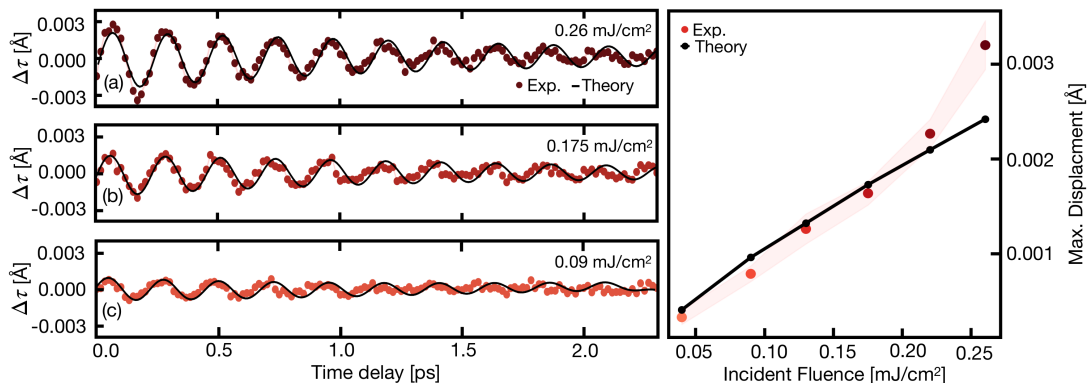


FIG. 6. (a-c) Comparison between theory and experiment for the displacement $\Delta\tau$ of Sb atoms from equilibrium due to the excitation the A_{1g} coherent phonon for fluences as indicated. (d) Comparison between theory and experiment for the maximum of the absolute displacement $|\Delta\tau|$ of Sb as a function of the incident fluence.

ample, is expected to induce dynamical renormalization of the Weyl points and their spin textures [20, 82, 83], with likely implications for topological properties [33] and transport anomalies [84]. Band engineering could further offer the opportunity to induced additional band crossings, leading to the dynamical formation of topological Weyl points in otherwise topologically trivial semimetals, or insulator-to-metal transitions in narrow-gap semiconductors [85]. More generally, the ab initio modelling of DECP in combination with tr-ARPES measurements can likely guide the identification of unexplored opportunities for engineering the band structure of semimetals via coherent phonons.

Besides band-structure engineering, the ab initio description of coherent phonons constitutes a powerful opportunity to monitor light-induced structural changes, which could shed light on the microscopic origin of light-induced phase transitions and symmetry breaking [39, 86]. By combining information from tr-ARPES and ab initio simulations, for example, one may directly retrieve the nuclear trajectories induced by coherent phonons. We illustrate this point in Fig. 6 (a-c), where we reconstructed the time-dependent displacement of Sb from equilibrium from tr-ARPES measurements. Here, the experimental displacement has been directly estimated from experiments via Eq. (1) as $\Delta\tau = (\hbar/2M_{\text{Sb}}\omega_\nu)^{\frac{1}{2}} e^\nu Q_\nu^{\text{exp}}(t)$ using the experimental coherent phonon amplitude $Q_\nu^{\text{exp}}(t) \simeq \langle \Delta\varepsilon_{n\mathbf{k}}^{\text{exp}}(t) \rangle / \langle g_{nn}^{\text{theo}}(\mathbf{k}, 0) \rangle$. In this expression, $\Delta\varepsilon_{n\mathbf{k}}^{\text{exp}}(t)$ denotes the measured band shift due to coherent phonons, $g_{nn}^{\text{theo}}(\mathbf{k}, 0)$ is the momentum-averaged coupling matrix elements obtained from ab initio calculations, and $\langle \dots \rangle$ indicates averaging over momentum. The calculated displacement, obtained from Eq. (2) is reported for comparison in Fig. 6, where we accounted for the experimental time resolution of $\Delta t = 100$ fs FWHM via a Gaussian convolution. We further illustrate in Fig. 6 (d) experimental and calculated maximum displacement as a function of pump fluence. This analysis indicates the possibility to directly determine the displacement of the nuclei from the exper-

imental data when the magnitude of the electron-phonon interaction is known from theory.

Another tr-ARPES study of Sb(111) provides additional experimental reference data for comparison with the results of our ab initio theory [70]. The paper reports a maximum oscillation amplitude in the Sb bulk band of about 3.3 meV (see Fig. 2(c) in Ref. [70]). For the incident fluence of 0.17 mJ cm^{-2} and considering the other experimental parameters [87], we estimate an absorbed fluence of 0.05 mJ cm^{-2} and calculate an oscillation amplitude of ≈ 4.7 meV for a sample temperature of 20 K in reasonable agreement with the experimental value. Similarly, our calculations for the displacement amplitude $\Delta\tau$ yield 0.15 pm which slightly overestimates the value ≈ 0.1 pm reported in Ref. [70].

While the Raman-active phonons excited via the DECP mechanism preserve the symmetry of the lattice, symmetry breaking could occur at high fluences via non-linear (ternary and quartic) phonon-phonon coupling mechanisms, such as, e.g., ionic Raman scattering. Overall, the ab initio approach developed here can be straightforwardly extended to account for these phenomena. It may thus offer new opportunities for crystal-structure control via non-linear phononics.

Finally, we emphasize that the solution of the coherent-phonon EOM (Eq. (2)) and the estimation of dynamical band-structure renormalization effects (Eqs. (6) and (7)) do not entail a significant increase in computational costs as compared to the solution of the TDBE (Eqs. (3) and (4)). Thus, the workflow presented in Fig. 2 for the simulation of coherent phonons can be promptly integrated into existing ab initio codes for electron-phonon coupling calculations, whenever Eqs. (3) and (4) are already available.

VIII. CONCLUSION

In conclusion, we reported a combined theoretical and experimental investigation of the light-induced structural

dynamics and electron-phonon interactions in driven semimetals. We formulated a transferable *ab initio* theory of the dispersive excitation of coherent phonons, which combines the time-dependent Boltzmann equation, the EOM for the coherent-phonon amplitude, and quasiparticle renormalization effects due to the polaron self-energy. Our approach specifically targets (i) the emergence of photo-induced coherent lattice motion following electronic excitation by a pump pulse and (ii) transient band-structure renormalization effects induced by coherent phonons. The points (i-ii) are a direct manifestation of the electron-phonon interactions occurring under non-equilibrium conditions, and their description eludes the capability of the equilibrium many-body approaches to the electron-phonon coupling.

We validated and benchmarked this approach against tr-ARPES experiments for the elemental semimetal antimony. To enable a quantitative comparison between experiment and theory, we detected and characterized the transient oscillations of the measured spectral function induced by coherent phonons for a wide range of pump fluences. We further conducted a frequency-domain analysis of coherent phonon oscillation (FD-ARPES), to deduce momentum- and mode-resolved information on the electron-phonon interactions. The good qualitative and quantitative agreement between measurements and simulations corroborate our *ab initio* approach. We further demonstrate the possibility to directly retrieve, via a combined experimental-theory approach, information about the electron-phonon coupling matrix elements and the nuclear trajectories from the tr-ARPES data.

Overall, the combination of *ab initio* theory and tr-ARPES emerges as a powerful diagnostic framework to directly characterize the light-induced structural changes and quasiparticle-energy renormalization in driven semimetals. We are confident that these advancements will open up opportunities for dynamical structural control and band-structure engineering.

ACKNOWLEDGMENTS

This work was funded by the Deutsche Forschungsgemeinschaft (DFG), Projects No. 499426961 and 443988403. The authors gratefully acknowledge the computing time provided by the high-performance computer Lichtenberg at the NHR Centers NHR4CES at TU Darmstadt (Project p0021280). F.C. acknowledges discussions with Elia Stocco.

APPENDIX

Appendix A: Computational details

1. Ground-state properties

DFT calculations are conducted with the plane-wave pseudopotential code `Quantum ESPRESSO` [58, 59]. Fully-relativistic projector augmented wave (PAW) pseudopotentials [88] and the Perdew-Burke-Ernzerhof (PBE) generalized-gradient approximation [89] for the exchange-correlation functional are used. The plane-wave kinetic-energy cutoff is set to 50 Ry, and the BZ is sampled with a $10 \times 10 \times 8$ Monkhorst-Pack grid. The phonon dispersion is obtained from DFPT on a $5 \times 5 \times 4$ q-point mesh [60]. Spin-orbit coupling (SOC) is included throughout all steps of the calculations. The electron and phonon eigenvalues, as well as the electron-phonon coupling matrix, are interpolated on a dense $40 \times 40 \times 15$ grid via maximally-localized Wannier functions [61] within `EPW` code [57], which uses `Wannier90` as a library [63].

2. Ultrafast dynamics from the TDBE

Equations (2)-(4) have been implemented in a modified version of the `EPW` code, and solved within an energy window of 1.5 eV around the Fermi energy. Time propagation is achieved by discretization of the time derivative via Heun's method for a total simulation time of 10 ps with a time step of 1 fs. The electron and phonon collision integrals due to the electron-phonon interaction ($\Gamma_{n\mathbf{k}}^{e-\text{ph}}$ and $\Gamma_{\mathbf{q}\nu}^{\text{ph}-e}$) are evaluated at each time-step on dense \mathbf{k} - and \mathbf{q} -grids of $40 \times 40 \times 15$, using a broadening of 10 meV for the numerical evaluation of the Dirac δ function. Explicit expressions for the collision integrals $\Gamma_{n\mathbf{k}}^{e-\text{ph}}$ and $\Gamma_{\mathbf{q}\nu}^{\text{ph}-e}$ and a detailed description of the computational procedure for their solution is reported elsewhere [49, 51]. We account for electron-electron scattering within the relaxation-time approximation via the inclusion of the collision integral:

$$\Gamma^{e-e}[f_{n\mathbf{k}}] = \frac{f_{n\mathbf{k}}(t) - f_{n\mathbf{k}}^{\text{eq}}(t)}{\tau^{e-e}} .$$

Here, $f_{n\mathbf{k}}^{\text{eq}}(t)$ is the equilibrium (Fermi-Dirac) distribution function at time t . To ensure energy conservation, $f_{n\mathbf{k}}^{\text{eq}}(t)$ is determined at each time step via the requirement that it yields an electronic energy $E_{\text{el}} = N_p^{-1} \sum_{n\mathbf{k}} \varepsilon_{n\mathbf{k}} f_{n\mathbf{k}}^{\text{eq}}$ which coincides with the one corresponding to the non-equilibrium distribution function $f_{n\mathbf{k}}(t)$. We set the average electron lifetime due to electron-electron interaction to $\tau^{e-e} \simeq 10$ meV. This value was deduced by averaging the imaginary part of the *GW* self-energy, as obtained from the `yambo` code [90], in an energy window of 1.5 eV around the Fermi energy. Simulations of the coherent-phonon dynamics are robust against changes of τ^{e-e} .

The phonon decoherence time of the A_{1g} -mode was

obtained estimated via the following expression:[49]

$$\frac{1}{\tau_{\mathbf{q}\nu}^{\text{PP}}} = \frac{\pi\hbar}{4} \sum_{\nu'\nu''} \int \frac{d\mathbf{q}'}{\Omega_{\text{BZ}}} \left| \Psi_{\mathbf{q}\mathbf{q}'\mathbf{q}''}^{\nu\nu'\nu''} \right|^2 [(n_{\mathbf{q}'\nu'} - n_{\mathbf{q}''\nu''})\delta(\omega_{\mathbf{q}\nu} + \omega_{\mathbf{q}'\nu'} - \omega_{\mathbf{q}''\nu''})\delta_{\mathbf{q}\mathbf{q}'-\mathbf{q}''}^{\text{G}} + (n_{\mathbf{q}'\nu'} + n_{\mathbf{q}''+1\nu''})\delta(\omega_{\mathbf{q}\nu} - \omega_{\mathbf{q}'\nu'} - \omega_{\mathbf{q}''\nu''})\delta_{\mathbf{q}-\mathbf{q}'-\mathbf{q}''}^{\text{G}}] \quad . \quad (\text{A1})$$

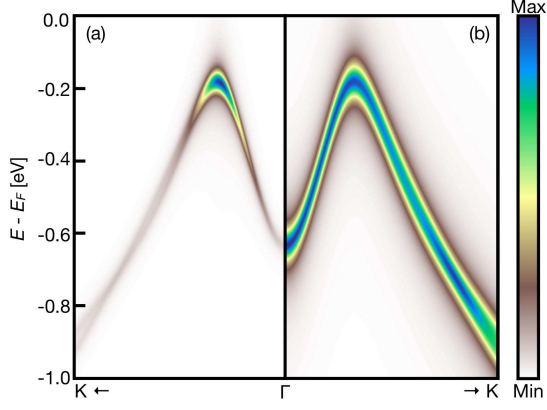


FIG. 7. Static electron spectral function for the bulk band of Sb due to the electron-phonon interaction in the Fan-Migdal approximation evaluated (a) with and (b) without dipole matrix elements for p-polarized light.

Here $\Psi_{\mathbf{q}\mathbf{q}'\mathbf{q}''}^{\nu\nu'\nu''}$ is the phonon-phonon coupling matrix element, which we evaluated for the A_{1g} -mode at Γ . The third-order force constant required for the estimation of $\Psi_{\mathbf{q}\mathbf{q}'\mathbf{q}''}^{\nu\nu'\nu''}$ has evaluated from difference based on the utility `third-order.py` [91]. Evaluation of Eq. (A1) yields $\tau_{A_{1g}}^{\text{PP}} = 2$ ps for antimony at room temperature. This value is kept constant throughout the simulations.

To account for the effects of optical selection rules arising from the polarization of the probe pulse, we evaluate the electron spectral function via [92]:

$$A(\omega, t) = \sum_{n\mathbf{k}}^{\text{occ}} \sum_{m\mathbf{k}}^{\text{unocc}} \frac{\pi^{-1} |d_{nm\mathbf{k}}|^2 \text{Im} \Sigma_{n\mathbf{k}}}{[\hbar\omega - \varepsilon_{n\mathbf{k}} - \text{Re} \Sigma_{n\mathbf{k}}]^2 + [\text{Im} \Sigma_{n\mathbf{k}}]^2} \quad ,$$

where $d_{nm\mathbf{k}} = \hat{\mathbf{e}} \cdot \langle u_{m\mathbf{k}} | \hat{\mathbf{p}} | u_{n\mathbf{k}} \rangle$ are the dipole transition probabilities, which we obtained from a modified version of the utility `epsilon.x`, part of **Quantum Espresso**. Here, $\hat{\mathbf{e}}$ denotes the light-polarization vector, $u_{n\mathbf{k}}$ the cell-periodic part of Kohn-Sham Bloch eigenstate, and $\hat{\mathbf{p}}$ the momentum operator. The effect of dipole transition probabilities for p-polarized light on the spectral function is illustrated in Fig. 7. The left (right) panel shows the spectral function with (without) dipole transition probabilities. The dipole transition probabilities suppress intensity away from the Γ point.

Appendix B: Initial conditions of ultrafast dynamics simulations

The initial condition for the numerical solution of Eqs. (2)-(4) is a Fermi-Dirac distribution $f_{n\mathbf{k}}^{\text{FD}}(T_{\text{exc}}) = \{\exp[(\varepsilon_{n\mathbf{k}} - \mu)/k_B T_{\text{exc}}] + 1\}^{-1}$ evaluated at the effective electronic temperature T_{exc} , where μ denotes the chemical potential, and k_B the Boltzmann constant. The lattice is initially at thermal equilibrium at room temperature ($T_0 = 300$ K), which coincides with the experimental conditions. Correspondingly, the initial ($t = 0$) phonon occupations are set by the Bose-Einstein statistics according to $n_{\mathbf{q}\nu}(t = 0) = [\exp(\hbar\omega_{\mathbf{q}\nu}/k_B T_0) - 1]^{-1}$.

The initial electronic temperature T_{exc} is determined as a function of the incident fluence employed in the experiments on the basis of the following rationale. The relation between the incident fluence F and the average increase of electronic energy per unit cell ΔE_{el} due to the pump absorption is given by:

$$\alpha F = d_z \Omega^{-1} \Delta E_{\text{el}} \quad . \quad (\text{B1})$$

Here, Ω is the volume of the unit cell, $d_z = 15$ nm is the penetration depth of the pump pulse, which we estimate from the extinction coefficient κ via:

$$d_z = \frac{\lambda}{4\pi\kappa} \quad . \quad (\text{B2})$$

With a wavelength of the laser light of $\lambda = 800$ nm and an extinction coefficient of $\kappa = 4.0803$ [65]. Furthermore, $\alpha = 0.4$ denotes the ratio between incident and absorbed fluence, which we obtain from the experimental absorption coefficient of Sb [65].

For the numerical solution of Eqs. (2)-(4), we define the initial electronic occupations $f_{n\mathbf{k}}(t = 0)$ such that they yield an excess electronic energy per unit cell coinciding with $\Delta E_{\text{el}} = \alpha \Omega F / d_z$ and are thus in compliance with Eq. (B1). In particular, we express the electron excited-state energy as

$$\Delta E_{\text{el}} = N_p^{-1} \sum_{n\mathbf{k}} \varepsilon_{n\mathbf{k}} [f_{n\mathbf{k}}^{\text{FD}}(T_{\text{exc}}) - f_{n\mathbf{k}}^{\text{FD}}(T_0)] \quad . \quad (\text{B3})$$

Combining Eqs. (B1) and (B3) we obtain an explicit relation between T_{exc} and the fluence F , which we solve numerically to determine the effective temperature T_{exc} and the electronic distribution function $f_{n\mathbf{k}}^{\text{FD}}(T_{\text{exc}})$ corresponding to the experimental incident fluence. Figure 8

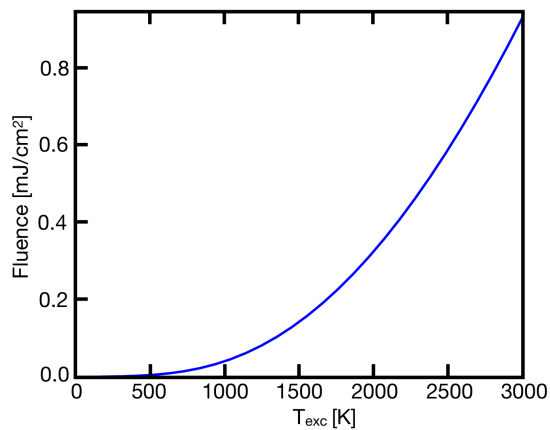


FIG. 8. Relation between the incident fluence and the effective electronic temperature T_{exc} obtained from numerical solution of Eqs. (B1) (B3) .

illustrates the relation between incident fluence and effective electron temperature T_{exc} obtained via this condition for antimony, considering an equilibrium temperature $T_0 = 300$ K.

We note that this Ansatz for the initial excited state is unsuitable to capture electron coherence and the emergence of nonthermal electronic states. These phenomena typically persist for 50-100 fs and can be systematically accounted for within a correlated description of the coupled electron-phonon dynamics based on non-equilibrium Green's functions.[54, 76, 93–95]

-
- [1] C. Thomsen, J. Strait, Z. Vardeny, H. J. Maris, J. Tauc, and J. Hauser, Coherent phonon generation and detection by picosecond light pulses, *Phys. Rev. Lett.* **53**, 989 (1984).
- [2] T. Cheng, S. Brorson, A. Kazeroonian, J. Moodera, G. Dresselhaus, M. Dresselhaus, and E. Ippen, Impulsive excitation of coherent phonons observed in reflection in bismuth and antimony, *Appl. Phys. Lett.* **57**, 1004 (1990).
- [3] T. K. Cheng, J. Vidal, H. J. Zeiger, G. Dresselhaus, M. S. Dresselhaus, and E. P. Ippen, Mechanism for displacive excitation of coherent phonons in Sb, Bi, Te, and Ti_2O_3 , *Appl. Phys. Lett.* **59**, 1923 (1991).
- [4] A. Kuznetsov and C. Stanton, Coherent phonon oscillations in GaAs, *Phys. Rev. B* **51**, 7555 (1995).
- [5] T. Dekorsy, H. Auer, C. Waschke, H. J. Bakker, H. G. Roskos, H. Kurz, V. Wagner, and P. Grosse, Emission of submillimeter electromagnetic waves by coherent phonons, *Phys. Rev. Lett.* **74**, 738 (1995).
- [6] M. Hase, K. Ishioka, J. Demsar, K. Ushida, and M. Kitajima, Ultrafast dynamics of coherent optical phonons and nonequilibrium electrons in transition metals, *Phys. Rev. B* **71**, 184301 (2005).
- [7] K. Ishioka, M. Kitajima, and O. V. Misochko, Coherent A_{1g} and E_g phonons of antimony, *J. Appl. Phys.* **103**, 123505 (2008).
- [8] R. P. Chatelain, V. R. Morrison, B. L. Klarenaar, and B. J. Siwick, Coherent and incoherent electron-phonon coupling in graphite observed with radio-frequency compressed ultrafast electron diffraction, *Phys. Rev. Lett.* **113**, 235502 (2014).
- [9] L. Waldecker, T. Vasileiadis, R. Bertoni, R. Ernstorfer, T. Zier, F. H. Valencia, M. E. Garcia, and E. S. Zijlstra, Coherent and incoherent structural dynamics in laser-excited antimony, *Phys. Rev. B* **95**, 054302 (2017).
- [10] S. Gerber, S.-L. Yang, D. Zhu, H. Soifer, J. A. Sobota, S. Rebec, J. J. Lee, T. Jia, B. Moritz, C. Jia, A. Gauthier, Y. Li, D. Leuenberger, Y. Zhang, L. Chaix, W. Li, H. Jang, J.-S. Lee, M. Yi, G. L. Dakovski, S. Song, J. M. Glowia, S. Nelson, K. W. Kim, Y.-D. Chuang, Z. Hussain, R. G. Moore, T. P. Devereaux, W.-S. Lee, P. S. Kirchmann, and Z.-X. Shen, Femtosecond electron-phonon lock-in by photoemission and x-ray free-electron laser, *Science* **357**, 71 (2017).
- [11] L. Perfetti, P. Loukakos, M. Lisowski, U. Bovensiepen, H. Berger, S. Biermann, P. Cornaglia, A. Georges, and M. Wolf, Time evolution of the electronic structure of 1T-TaS₂ through the insulator-metal transition, *Phys. Rev. Lett.* **97**, 067402 (2006).
- [12] J. Petersen, S. Kaiser, N. Dean, a. Simoncig, H. Liu, a. Cavalieri, C. Cacho, I. Turcu, E. Springate, F. Frassetto, L. Poletto, S. Dhesi, H. Berger, and a. Cavalleri, Clocking the Melting Transition of Charge and Lattice Order in 1T-TaS₂ with Ultrafast Extreme-Ultraviolet Angle-Resolved Photoemission Spectroscopy, *Phys. Rev. Lett.* **107**, 1 (2011).
- [13] S. Hellmann, T. Rohwer, M. Kalläne, K. Hanff, C. Sohrt, A. Stange, A. Carr, M. Murnane, H. Kapteyn, L. Kipp, M. Bauer, and K. Rossnagel, Time-domain classification of charge-density-wave insulators, *Nat. Commun.* **3**, 1069 (2012).
- [14] E. Papalazarou, J. Faure, J. Mauchain, M. Marsi, A. Taleb-Ibrahimi, I. Reshetnyak, A. Van Roekeghem, I. Timrov, N. Vast, B. Arnaud, and L. Perfetti, Coherent phonon coupling to individual bloch states in photoexcited bismuth, *Phys. Rev. Lett.* **108**, 256808 (2012).
- [15] J. A. Sobota, S.-L. Yang, D. Leuenberger, A. F. Kemper, J. G. Analytis, I. R. Fisher, P. S. Kirchmann, T. P. Devereaux, and Z.-X. Shen, Distinguishing bulk and surface electron-phonon coupling in the topological insulator Bi₂Se₃ using time-resolved photoemission spectroscopy, *Phys. Rev. Lett.* **113**, 157401 (2014).
- [16] L. Rettig, J.-H. Chu, I. Fisher, U. Bovensiepen, and M. Wolf, Coherent dynamics of the charge density wave gap in tritellurides, *Faraday Discuss.* **171**, 299 (2014).
- [17] E. Golias and J. Sánchez-Barriga, Observation of antiphase coherent phonons in the warped Dirac cone of Bi₂Te₃, *Phys. Rev. B* **94**, 161113(R) (2016).
- [18] T. Tang, H. Wang, S. Duan, Y. Yang, C. Huang, Y. Guo, D. Qian, and W. Zhang, Non-Coulomb

- strong electron-hole binding in Ta₂NiSe₅ revealed by time- and angle-resolved photoemission spectroscopy, *Phys. Rev. B* **101**, 235148 (2020).
- [19] E. Baldini, A. Zong, D. Choi, C. Lee, M. H. Michael, L. Windgatter, I. I. Mazin, S. Latini, D. Azoury, B. Lv, A. Kogar, Y. Su, Y. Wang, Y. Lu, T. Takayama, H. Takagi, A. J. Millis, A. Rubio, E. Demler, and N. Gedik, The spontaneous symmetry breaking in Ta₂NiSe₅ is structural in nature, *Proc. Natl. Acad. Sci.* **120**, 1 (2023).
- [20] P. Hein, S. Jauernik, H. Erk, L. Yang, Y. Qi, Y. Sun, C. Felser, and M. Bauer, Mode-resolved reciprocal space mapping of electron-phonon interaction in the Weyl semimetal candidate *Td*-WTe₂, *Nat. Commun.* **11**, 2613 (2020).
- [21] U. De Giovannini, H. Hübener, S. A. Sato, and A. Rubio, Direct measurement of electron-phonon coupling with time-resolved ARPES, *Phys. Rev. Lett.* **125**, 136401 (2020).
- [22] T. Suzuki, Y. Shinohara, Y. Lu, M. Watanabe, J. Xu, K. L. Ishikawa, H. Takagi, M. Nohara, N. Katayama, H. Sawa, M. Fujisawa, T. Kanai, J. Itatani, T. Mizokawa, S. Shin, and K. Okazaki, Detecting electron-phonon coupling during photoinduced phase transition, *Phys. Rev. B* **103**, L121105 (2021).
- [23] W. Lee, S. Fernandez-Mulligan, H. Tan, C. Yan, Y. Guan, S. H. Lee, R. Mei, C. Liu, B. Yan, Z. Mao, and S. Yang, Layer-by-layer disentanglement of Bloch states, *Nat. Phys.* **19**, 950 (2023).
- [24] Q. Ren, T. Suzuki, T. Kanai, J. Itatani, S. Shin, and K. Okazaki, Phase-resolved frequency-domain analysis of the photoemission spectra for photoexcited 1T-TaS₂ in the Mott insulating charge density wave state, *Appl. Phys. Lett.* **122**, 221902 (2023).
- [25] S. Wall, D. Prabhakaran, A. Boothroyd, and A. Cavalleri, Ultrafast coupling between light, coherent lattice vibrations, and the magnetic structure of semicovalent LaMnO₃, *Phys. Rev. Lett.* **103**, 097402 (2009).
- [26] K. W. Kim, A. Pashkin, H. Schäfer, M. Beyer, M. Porer, T. Wolf, C. Bernhard, J. Demsar, R. Huber, and A. Leitenstorfer, Ultrafast transient generation of spin-density-wave order in the normal state of BaFe₂As₂ driven by coherent lattice vibrations, *Nat. Mater.* **11**, 497 (2012).
- [27] T. F. Nova, A. Cartella, A. Cantaluppi, M. Först, D. Bossini, R. V. Mikhaylovskiy, A. V. Kimel, R. Merlin, and A. Cavalleri, An effective magnetic field from optically driven phonons, *Nat. Phys.* **13**, 132 (2017).
- [28] D. Afanasiev, J. R. Hortensius, B. A. Ivanov, A. Sasani, E. Bousquet, Y. M. Blanter, R. V. Mikhaylovskiy, A. V. Kimel, and A. D. Caviglia, Ultrafast control of magnetic interactions via light-driven phonons, *Nat. Mater.* **20**, 607 (2021).
- [29] H. Bakker, S. Hunsche, and H. Kurz, Coherent phonon polaritons as probes of anharmonic phonons in ferroelectrics, *Rev. Mod. Phys.* **70**, 523 (1998).
- [30] D. M. Juraschek, M. Fechner, A. V. Balatsky, and N. A. Spaldin, Dynamical multiferroicity, *Phys. Rev. Mater.* **1**, 014401 (2017).
- [31] R. Mankowsky, A. von Hoegen, M. Först, and A. Cavalleri, Ultrafast reversal of the ferroelectric polarization, *Phys. Rev. Lett.* **118**, 197601 (2017).
- [32] M. Fechner, M. Först, G. Orenstein, V. Krapivin, A. S. Disa, M. Buzzi, A. Von Hoegen, G. De La Pena, Q. L. Nguyen, R. Mankowsky, M. Sander, H. Lemke, Y. Deng, M. Trigo, and A. Cavalleri, Quenched lattice fluctuations in optically driven SrTiO₃, *Nat. Mater.* **23**, 363 (2024).
- [33] E. J. Sie, C. M. Nyby, C. D. Pemmaraju, S. J. Park, X. Shen, J. Yang, M. C. Hoffmann, B. K. Ofori-Okai, R. Li, A. H. Reid, S. Weathersby, E. Mannebach, N. Finney, D. Rhodes, D. Chenet, A. Antony, L. Balicas, J. Hone, T. P. Devereaux, T. F. Heinz, X. Wang, and A. M. Lindenberg, An ultrafast symmetry switch in a Weyl semimetal, *Nature* **565**, 61 (2019).
- [34] R. Mankowsky, A. Subedi, M. Först, S. O. Mariager, M. Chollet, H. T. Lemke, J. S. Robinson, J. M. Glownia, M. P. Minitti, A. Frano, M. Fechner, N. A. Spaldin, T. Loew, B. Keimer, A. Georges, and A. Cavalleri, Nonlinear lattice dynamics as a basis for enhanced superconductivity in YBa₂Cu₃O_{6.5}, *Nature* **516**, 71 (2014).
- [35] B. Liu, M. Först, M. Fechner, D. Nicoletti, J. Porras, T. Loew, B. Keimer, and A. Cavalleri, Pump frequency resonances for light-induced incipient superconductivity in yba₂cu₃o_{6.5}, *Phys. Rev. X* **10**, 011053 (2020).
- [36] M. Mitrano, A. Cantaluppi, D. Nicoletti, S. Kaiser, A. Perucchi, S. Lupi, P. Di Pietro, D. Pontiroli, M. Riccò, S. R. Clark, D. Jaksch, and A. Cavalleri, Possible light-induced superconductivity in K₃C₆₀ at high temperature, *Nature* **530**, 461 (2016).
- [37] D. M. Juraschek, M. Fechner, and N. A. Spaldin, Ultrafast structure switching through nonlinear phononics, *Phys. Rev. Lett.* **118**, 054101 (2017).
- [38] A. De La Torre, D. M. Kennes, M. Claassen, S. Gerber, J. W. McIver, and M. A. Sentef, Colloquium: Nonthermal pathways to ultrafast control in quantum materials, *Rev. Mod. Phys.* **93**, 041002 (2021).
- [39] S. Mocatti, G. Marini, and M. Calandra, Light-induced nonthermal phase transition to the topological crystalline insulator state in SnSe, *J. Phys. Chem. Lett.* **14**, 9329 (2023).
- [40] L. Yang, G. Rohde, Y. Chen, W. Shi, Z. Liu, F. Chen, Y. Chen, K. Rossnagel, and M. Bauer, Experimental evidence for a metastable state in FeTe_{1-x}Se_x following coherent-phonon excitation, *J. Electron Spectros. Relat. Phenomena* **250**, 147085 (2021).
- [41] H. Zeiger, J. Vidal, T. Cheng, E. Ippen, G. Dresselhaus, and M. Dresselhaus, Theory for displacive excitation of coherent phonons, *Phys. Rev. B* **45**, 768 (1992).
- [42] A. V. Kuznetsov and C. J. Stanton, Theory of coherent phonon oscillations in semiconductors, *Phys. Rev. Lett.* **73**, 3243 (1994).
- [43] L. Dhar, J. A. Rogers, and K. A. Nelson, Time-resolved vibrational spectroscopy in the impulsive limit, *Chem. Rev.* **94**, 157 (1994).
- [44] Y. Giret, A. Gellé, and B. Arnaud, Entropy driven atomic motion in laser-excited bismuth, *Phys. Rev. Lett.* **106**, 155503 (2011).
- [45] D. M. Juraschek and S. F. Maehrlein, Sum-frequency ionic raman scattering, *Phys. Rev. B* **97**, 174302 (2018).
- [46] M. Lakehal and I. Paul, Microscopic description of displacive coherent phonons, *Phys. Rev. B* **99**, 035131 (2019).
- [47] F. Caruso and M. Zacharias, Quantum theory of light-driven coherent lattice dynamics, *Phys. Rev. B* **107**, 054102 (2023).
- [48] G. A. Garrett, T. F. Albrecht, J. F. Whitaker, and R. Merlin, Coherent thz phonons driven by light pulses and the Sb problem: What is the mechanism?, *Phys. Rev. Lett.* **77**, 3661 (1996).
- [49] F. Caruso, Nonequilibrium lattice dynamics in monolayer

- MoS₂, *J. Phys. Chem. Lett.* **12**, 1734 (2021).
- [50] X. Tong and M. Bernardi, Toward precise simulations of the coupled ultrafast dynamics of electrons and atomic vibrations in materials, *Phys. Rev. Res.* **3**, 023072 (2021).
- [51] F. Caruso and D. Novko, Ultrafast dynamics of electrons and phonons: from the two-temperature model to the time-dependent Boltzmann equation, *Adv. Phys.: X* **7**, 2095925 (2022).
- [52] Y. Pan and F. Caruso, Vibrational dichroism of chiral valley phonons, *Nano Lett.* **23**, 7463 (2023).
- [53] F. Giustino, Electron-phonon interactions from first principles, *Rev. Mod. Phys.* **89**, 015003 (2017).
- [54] G. Stefanucci, R. van Leeuwen, and E. Perfetto, In and out-of-equilibrium ab initio theory of electrons and phonons, *Phys. Rev. X* **13**, 031026 (2023).
- [55] E. Perfetto, K. Wu, and G. Stefanucci, Theory of coherent phonons coupled to excitons, *npj 2D mater. appl.* **8**, 40 (2024).
- [56] B. Rethfeld, A. Kaiser, M. Vicanek, and G. Simon, Ultrafast dynamics of nonequilibrium electrons in metals under femtosecond laser irradiation, *Phys. Rev. B* **65**, 214303 (2002).
- [57] H. Lee, S. Poncé, K. Bushick, S. Hajinazar, J. Lafuente-Bartolome, J. Leveillee, C. Lian, J.-M. Lihm, F. Macheda, H. Mori, H. Paudyal, W. H. Sio, S. Tiwari, M. Zacharias, X. Zhang, N. Bonini, E. Kioupakis, E. R. Margine, and F. Giustino, Electron-phonon physics from first principles using the EPW code, *npj Comput. Mater.* **9**, 156 (2023).
- [58] P. Giannozzi, S. Baroni, N. Bonini, M. Calandra, R. Car, C. Cavazzoni, D. Ceresoli, G. L. Chiarotti, M. Cococcioni, I. Dabo, A. D. Corso, S. de Gironcoli, S. Fabris, G. Fratesi, R. Gebauer, U. Gerstmann, C. Gougoussis, A. Kokalj, M. Lazzeri, L. Martin-Samos, N. Marzari, F. Mauri, R. Mazzarello, S. Paolini, A. Pasquarello, L. Paulatto, C. Sbraccia, S. Scandolo, G. Sclauzero, A. P. Seitsonen, A. Smogunov, P. Umari, and R. M. Wentzcovitch, **Quantum ESPRESSO**: a modular and open-source software project for quantum simulations of materials, *J. Phys. Condens. Matter* **21**, 395502 (2009).
- [59] P. Giannozzi, O. Andreussi, T. Brumme, O. Bunau, M. B. Nardelli, M. Calandra, R. Car, C. Cavazzoni, D. Ceresoli, M. Cococcioni, *et al.*, Advanced capabilities for materials modelling with **Quantum ESPRESSO**, *J. Phys. Condens. Matter* **29**, 465901 (2017).
- [60] S. Baroni, S. De Gironcoli, A. Dal Corso, and P. Giannozzi, Phonons and related crystal properties from density-functional perturbation theory, *Rev. Mod. Phys.* **73**, 515 (2001).
- [61] N. Marzari, A. A. Mostofi, J. R. Yates, I. Souza, and D. Vanderbilt, Maximally localized Wannier functions: Theory and applications, *Rev. Mod. Phys.* **84**, 1419 (2012).
- [62] F. Giustino, M. L. Cohen, and S. G. Louie, Electron-phonon interaction using Wannier functions, *Phys. Rev. B* **76**, 165108 (2007).
- [63] G. Pizzi, V. Vitale, R. Arita, S. Blügel, F. Freimuth, G. Géranton, M. Gibertini, D. Gresch, C. Johnson, T. Koretsune, J. Ibañez-Azpiroz, H. Lee, J.-M. Lihm, D. Marchand, A. Marrazzo, Y. Mokrousov, J. I. Mustafa, Y. Nohara, Y. Nomura, L. Paulatto, S. Poncé, T. Ponce, J. Qiao, F. Thöle, S. S. Tsirkin, M. Wierzbowska, N. Marzari, D. Vanderbilt, I. Souza, A. A. Mostofi, and J. R. Yates, **Wannier90** as a community code: new features and applications, *J. Condens. Matter Phys.* **32**, 165902 (2020).
- [64] S. Jauernik, P. Hein, M. Gurgel, J. Falke, and M. Bauer, Probing long-range structural order in SnPc/Ag(111) by umklapp process assisted low-energy angle-resolved photoelectron spectroscopy, *Phys. Rev. B* **97**, 125413 (2018).
- [65] G. Hass and L. Hadley, Optical properties of metals, *American Institute of Physics Handbook* **2**, 6 (1972).
- [66] Y. Liu and R. E. Allen, Electronic structure of the semimetals Bi and Sb, *Phys. Rev. B* **52**, 1566 (1995).
- [67] E. S. Zijlstra, L. L. Tatarinova, and M. E. Garcia, Laser-induced phonon-phonon interactions in bismuth, *Phys. Rev. B* **74**, 220301 (2006).
- [68] See Supplemental Material at URL-will-be-inserted-by-publisher, which include Supplementary Note S1, Supplementary Figures S1-S7, one Supplementary Video and citations to Ref. [96, 97].
- [69] O. J. Clark, F. Freyse, I. Aguilera, A. S. Frolov, A. M. Ionov, S. I. Bozhko, L. V. Yashina, and J. Sánchez-Barriga, Observation of a giant mass enhancement in the ultrafast electron dynamics of a topological semimetal, *Commun. Phys.* **4**, 165 (2021).
- [70] S. Sakamoto, N. Gauthier, P. S. Kirchmann, J. A. Sobota, and Z.-X. Shen, Connection between coherent phonons and electron-phonon coupling in Sb (111), *Phys. Rev. B* **105**, L161107 (2022).
- [71] M. Lax, Quantum relaxation, the shape of lattice absorption and inelastic neutron scattering lines, *J. Phys. Chem. Solids* **25**, 487 (1964).
- [72] M. Hase, K. Mizoguchi, H. Harima, S.-i. Nakashima, and K. Sakai, Dynamics of coherent phonons in bismuth generated by ultrashort laser pulses, *Phys. Rev. B* **58**, 5448 (1998).
- [73] K. Ishioka, M. Hase, M. Kitajima, and K. Ushida, Ultrafast carrier and phonon dynamics in ion-irradiated graphite, *Appl. Phys. Lett.* **78**, 3965 (2001).
- [74] S. Fahy, É. D. Murray, and D. A. Reis, Resonant squeezing and the anharmonic decay of coherent phonons, *Phys. Rev. B* **93**, 134308 (2016).
- [75] J. Lafuente-Bartolome, C. Lian, W. H. Sio, I. G. Gurtubay, A. Eiguren, and F. Giustino, Unified approach to polarons and phonon-induced band structure renormalization, *Phys. Rev. Lett.* **129**, 076402 (2022).
- [76] G. Stefanucci and E. Perfetto, Semiconductor electron-phonon equations: A rung above Boltzmann in the many-body ladder, *SciPost Phys.* **16**, 073 (2024).
- [77] J. Lafuente-Bartolome, C. Lian, W. H. Sio, I. G. Gurtubay, A. Eiguren, and F. Giustino, Ab initio self-consistent many-body theory of polarons at all couplings, *Phys. Rev. B* **106**, 075119 (2022).
- [78] S. Poncé, E. R. Margine, C. Verdi, and F. Giustino, **EPW**: Electron-phonon coupling, transport and superconducting properties using maximally localized Wannier functions, *Comput. Phys. Commun.* **209**, 116 (2016).
- [79] F. Caruso, M. Hoesch, P. Achatz, J. Serrano, M. Krisch, E. Bustarret, and F. Giustino, Nonadiabatic Kohn anomaly in heavily boron-doped diamond, *Phys. Rev. Lett.* **119**, 017001 (2017).
- [80] D. Novko, F. Caruso, C. Draxl, and E. Cappelluti, Ultrafast hot phonon dynamics in MgB₂ driven by anisotropic electron-phonon coupling,

- Phys. Rev. Lett. **124**, 077001 (2020).
- [81] D. Fausti, O. V. Misochko, and P. H. van Loosdrecht, Ultrafast photoinduced structure phase transition in antimony single crystals, Phys. Rev. B **80**, 161207 (2009).
- [82] M. Sakano, M. Hirayama, T. Takahashi, S. Akebi, M. Nakayama, K. Kuroda, K. Taguchi, T. Yoshikawa, K. Miyamoto, T. Okuda, K. Ono, H. Kumigashira, T. Ideue, Y. Iwasa, N. Mitsuishi, K. Ishizaka, S. Shin, T. Miyake, S. Murakami, T. Sasagawa, and T. Kondo, Radial spin texture in elemental tellurium with chiral crystal structure, Phys. Rev. Lett. **124**, 136404 (2020).
- [83] G. Gatti, D. Gosálbez-Martínez, S. Tsirkin, M. Fanciulli, M. Puppini, S. Polishchuk, S. Moser, L. Testa, E. Martino, S. Roth, P. Bugnon, L. Moreschini, A. Bostwick, C. Jozwiak, E. Rotenberg, G. Di Santo, L. Petaccia, I. Vobornik, J. Fujii, J. Wong, D. Jariwala, H. Atwater, H. Rønnow, M. Chergui, O. Yazyev, M. Grioni, and A. Crepaldi, Radial spin texture of the Weyl fermions in chiral tellurium, Phys. Rev. Lett. **125**, 216402 (2020).
- [84] B. Yan and C. Felser, Topological materials: Weyl semimetals, Annu. Rev. Condens. Matter Phys. **8**, 337 (2017).
- [85] H. Ning, O. Mehio, C. Lian, X. Li, E. Zoghlin, P. Zhou, B. Cheng, S. D. Wilson, B. M. Wong, and D. Hsieh, Light-induced Weyl semiconductor-to-metal transition mediated by Peierls instability, Phys. Rev. B **106**, 205118 (2022).
- [86] M.-X. Guan, X.-B. Liu, D.-Q. Chen, X.-Y. Li, Y.-P. Qi, Q. Yang, P.-W. You, and S. Meng, Optical control of multistage phase transition via phonon coupling in MoTe₂, Phys. Rev. Lett. **128**, 015702 (2022).
- [87] A. Gauthier, J. A. Sobota, N. Gauthier, K.-J. Xu, H. Pfau, C. R. Rotundu, Z.-X. Shen, and P. S. Kirchmann, Tuning time and energy resolution in time-resolved photoemission spectroscopy with nonlinear crystals, J. Appl. Phys. **128** (2020).
- [88] A. Dal Corso, Pseudopotentials periodic table: From H to Pu, Comput. Mater. Sci. **95**, 337 (2014).
- [89] J. P. Perdew, K. Burke, and M. Ernzerhof, Generalized gradient approximation made simple, Phys. Rev. Lett. **77**, 3865 (1996).
- [90] D. Sangalli, A. Ferretti, H. Miranda, C. Attaccalite, I. Marri, E. Cannuccia, P. Melo, M. Marsili, F. Paleari, A. Marrazzo, G. Prandini, P. Bonfà, M. O. Atambo, F. Affinito, M. Palumbo, A. Molina-Sánchez, C. Hogan, M. Grüning, D. Varsano, and A. Marini, Many-body perturbation theory calculations using the **yambo** code, J. Condens. Matter Phys. **31**, 325902 (2019).
- [91] W. Li, J. Carrete, N. A. Katcho, and N. Mingo, **ShengBTE**: a solver of the Boltzmann transport equation for phonons, Comp. Phys. Commun. **185**, 1747 (2014).
- [92] S. Moser, An experimentalist's guide to the matrix element in angle-resolved photoemission, J. Electron Spectros. Relat. Phenomena **214**, 29 (2017).
- [93] E. Perfetto and G. Stefanucci, Real-time GW-Ehrenfest-Fan-Migdal method for nonequilibrium 2D materials, Nano Lett. **23**, 7029 (2023).
- [94] D. Karlsson, R. van Leeuwen, Y. Pavlyukh, E. Perfetto, and G. Stefanucci, Fast Green's function method for ultrafast electron-Boson dynamics, Phys. Rev. Lett. **127**, 036402 (2021).
- [95] A. Molina-Sánchez, D. Sangalli, L. Wirtz, and A. Marini, Ab initio calculations of ultrashort carrier dynamics in two-dimensional materials: Valley depolarization in single-layer WSe₂, Nano Lett. **17**, 4549 (2017).
- [96] D. Campi, M. Bernasconi, and G. Benedek, Phonons and electron-phonon interaction at the Sb (111) surface, Phys. Rev. B **86**, 075446 (2012).
- [97] W. Setyawan and S. Curtarolo, High-throughput electronic band structure calculations: Challenges and tools, Comput. Mater. Sci. **49**, 299 (2010).